Active quantum flocks

Reyhaneh Khasseh, Sascha Wald, Roderich Moessner, Christoph A. Weber, Markus Heyl

Angaben zur Veröffentlichung / Publication details:

Khasseh, Reyhaneh, Sascha Wald, Roderich Moessner, Christoph A. Weber, and Markus Heyl. 2025. "Active quantum flocks." *Physical Review Letters* 135 (24): 248302. https://doi.org/10.1103/rd46-hr3q.

Active Quantum Flocks

Reyhaneh Khasseh,[1,2] Sascha Wald,[3] Roderich Moessner,[2] Christoph A. Weber,[4,2] and Markus Heyl[1,2]
[1]Theoretical Physics III, Center for Electronic Correlations and Magnetism, Institute of Physics, University of Augsburg, D-86135 Augsburg, Germany
[2]Max-Planck-Institut für Physik komplexer Systeme, 01187 Dresden, Germany
[3]Statistical Physics Group, Centre for Fluid and Complex Systems, Coventry University, Coventry, United Kingdom
[4]Faculty of Mathematics, Natural Sciences, and Materials Engineering: Institute of Physics, University of Augsburg, Universitätsstraße 1, 86159 Augsburg, Germany

(Received 5 June 2025; accepted 14 November 2025; published 10 December 2025)

Flocks of animals represent a prominent archetype of collective behavior in the macroscopic classical world, where the constituents, such as birds, concertedly perform motions and actions as if being one single entity. Here, we address the so far open question of whether flocks can also form in the microscopic world at the quantum level. For that purpose, we introduce the concept of *active quantum matter* by formulating a class of models of active quantum particles on a one-dimensional lattice. We provide both analytical and large-scale numerical evidence that these systems can give rise to quantum flocks. A key finding is that these quantum flocks exhibit distinct quantum properties by developing strong quantum coherence over long distances. We propose that quantum flocks could be experimentally observed in Rydberg atom arrays.

DOI: 10.1103/rd46-hr3q

Introduction—In the quantum world, remarkable advances in quantum simulators have led to unprecedented capabilities in controlling and probing the real-time dynamics of quantum matter [1–4]. Among the most important developments have been the observation of genuinely nonequilibrium phases of matter such as many-body localization [5,6], discrete time crystals [7,8], or quantum many-body scars [9]. In the classical world, progress in the understanding of dynamical processes maintained away from equilibrium in the context of active matter systems, e.g., describing the physics of biological systems, has been distinctly impressive [10–15]. This, in particular, includes one of the most prominent archetypes of collective motion, flocks, which realize an oriented, clustered, and moving collection of constituents [16–18]. So far, these developments on the nonequilibrium many-body physics of quantum and classical systems have evolved independently, leaving open the fundamental question emerging naturally at their interface: is it also possible for quantum particles to exhibit flocking, similar to birds or fish in the classical world?

In this Letter, we introduce the concept of active quantum matter, by formulating key underlying quantum dynamical processes. We then provide evidence that these particles can realize a quantum flock in that they form collectively moving clusters that spontaneously undergo polar symmetry breaking. We observe that the resulting flock experiences distinct quantum features absent in the classical world. Specifically, our active quantum system exhibits a pronounced long-distance quantum coherence suggesting coherent, ballistic motion over large distances. We argue that the identified underlying mechanism is general and can also be potentially used to realize other phases of active quantum matter. Our Letter therefore opens up a route toward exploring yet unknown classes of nonequilibrium states in quantum many-body systems with the potential to also realize other collective behaviors of biological active matter systems in a quantum context.

Model for active quantum flocks—It is the key aim of this Letter to devise a quantum-mechanical analog of active matter systems [19,20], with the particular goal to realize flocks in the quantum world. For that purpose, it will be necessary to identify quantum counterparts to the following two processes. First, it would be key to determine how to make quantum particles active, which in analogy to the classical world would mean that their motion is continuously supplied with energy on the single-particle level from an environment, breaking local detailed balance and enabling persistent motion [11,12,21–23]. Second, in order for such active particles to form a flock, a so-called alignment process is required describing an interaction that correlates the particles' direction of motion according to their environment, such as birds aligning their velocity with their neighbors' in the pioneering Vicsek model [16].

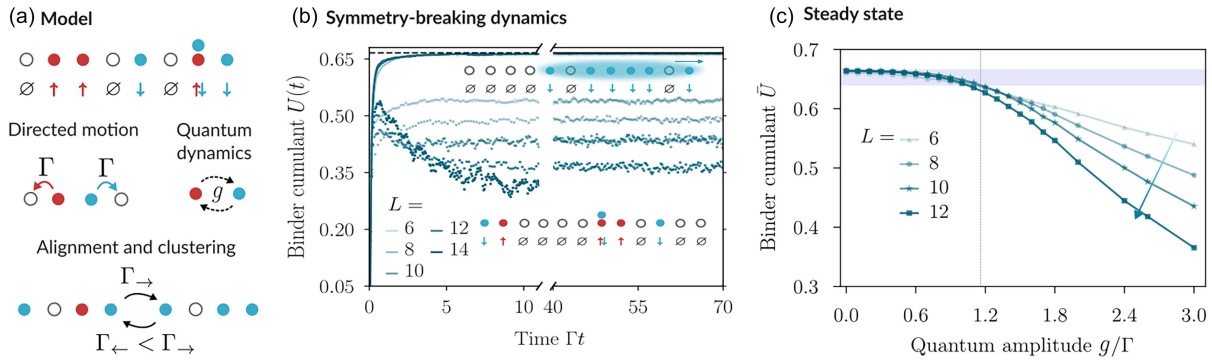

FIG. 1. Active quantum flocks. (a) The model for active quantum matter involves two species of hard-core bosons ($\uparrow, \downarrow$) on a one-dimensional lattice subject to three types of dynamical processes. The particles perform a dissipative directed motion at a rate Γ with $\uparrow$ and $\downarrow$ particles moving to the left and right, respectively. Quantum dynamics is introduced by a coherent spin-flip process occurring with an amplitude g. Alignment and clustering of particles is enabled by a conditional dissipative spin-flip process whose rate effectively depends on the surrounding magnetization. Here, the rate $\Gamma_{\leftarrow} < \Gamma_{\rightarrow}$ as the environment is dominated by $\downarrow$ particles. (b) Dynamics of the Binder cumulant $U(t)$ for different quantum amplitudes g indicating long-range order for weak $g = 0.2$ (solid lines), whereas for large $g = 3.0$ (dotted lines) the Binder cumulant exhibits a tendency toward a vanishing value upon increasing L suggesting a disordered phase. The numerical data have been obtained for an alignment parameter $K = 3.8$ and $N_r = 1000$ trajectories. (c) Long-time average of the Binder cumulant $\bar{U}$ as a function of the quantum amplitude g of the quantum dynamics for different system sizes L at alignment parameter $K = 3.8$. For weak g the Binder cumulant approaches a value of $U = 2/3$ indicative of a quantum flocking phase, whereas for large g the Binder cumulant displays a tendency toward a vanishing value upon increasing L. The horizontal shaded area indicates the threshold used to estimate the phase transition point, which is included as the dashed line.

This, however, imposes a direct challenge in the quantum world, since, quantum mechanically, positions and velocities (or momenta) are noncommuting observables.

In the following, we introduce a general class of quantum models that address these challenges. We consider a system of hard-core bosons on a one-dimensional chain of L lattice sites with periodic boundary conditions and two species of particles labeled by an effective spin $\sigma = \uparrow, \downarrow$ [see Fig. 1(a)]. In Supplemental Material, Sec. VIII [24], we discuss how to realize the individual dynamical processes microscopically in systems of Rydberg atoms.

It is key for active matter to include dissipative processes. We choose environments that can be effectively described by a Lindblad master equation [25],

$$\frac{d\hat{\rho}}{dt} = -i[\hat{H}, \hat{\rho}] + \mathcal{D}(\hat{\rho}), \tag{1}$$

which appear genuinely when coupling quantum matter to photons. Here, $\hat{\rho}$ denotes the density matrix of the quantum system. Two types of contributions can be distinguished, the coherent evolution by the Hamiltonian $\hat{H}$ and the dissipative dynamics generated through $\mathcal{D}(\hat{\rho})$.

We now introduce specific environments, which realize the aforementioned two key desired processes responsible, firstly, for the active motion (labeled by $X = \mathcal{M}$ in the following) and, secondly, for the alignment ($X = \mathcal{A}$). This leads to a decomposition $\mathcal{D}(\hat{\rho}) = \mathcal{D}_{\mathcal{M}}(\hat{\rho}) + \mathcal{D}_{\mathcal{A}}(\hat{\rho})$, where $\mathcal{D}_X(\hat{\rho}) = \sum_{l=1}^{L} \sum_{\sigma=\uparrow,\downarrow} (\Gamma_X/2)(2\hat{X}_{l\sigma}\hat{\rho}\hat{X}_{l\sigma}^{\dagger} - \hat{X}_{l\sigma}^{\dagger}\hat{X}_{l\sigma}\hat{\rho} - \hat{\rho}\hat{X}_{l\sigma}^{\dagger}\hat{X}_{l\sigma})$. Here, $\hat{X}_{l\sigma}$ denotes the respective quantum jump operator of species σ on lattice site l, and Γ_X is the rate of the corresponding process. An alternative formulation of the dissipative contributions is discussed in Supplemental Material, Sec. VI [24].

In order to make the system active we choose quantum jump operators $\hat{\mathcal{M}}_{l\uparrow} = \hat{c}_{l\uparrow}^{\dagger}\hat{c}_{l+1\uparrow}$, $\hat{\mathcal{M}}_{l\downarrow} = \hat{c}_{l+1\downarrow}^{\dagger}\hat{c}_{l\downarrow}$. Here, $\hat{c}_{l\sigma}^{\dagger}$ denotes the creation operator for a hard-core boson of type σ at lattice site l. This contribution leads to a directed motion of spin-$\uparrow$ and $\downarrow$ particles to the left and right, respectively, in close analogy to classical active Ising models [19,20]. Importantly, this dynamical process violates Kolmogorov's criterion implying the breaking of local detailed balance (see Supplemental Material, Sec. I [24]). While recent works have already aimed at identifying active quantum processes for single particles [26,27], the process presented here induces activity on a many-body level.

In a next step we now aim to address the challenge of realizing a local alignment of velocities. For that purpose, we introduce a dissipative process aligning locally the internal degree of freedom σ of the particles, which in turn also aligns their direction of motion. Concretely, we choose $\hat{\mathcal{A}}_{l\sigma} = \hat{c}_{l\sigma}^{\dagger}\hat{c}_{l\bar{\sigma}}\hat{P}_l$ inducing transitions between the two particle species. Here, $\bar{\sigma}$ denotes the spin species with opposite orientation to σ. The key alignment property is contained in $\hat{P}_l$, which is designed to make the process conditional on a surrounding magnetization in such a way that spin-changing processes for a particle are suppressed or enhanced when the spin of the particle does or does not align with the neighborhood, respectively. This can be achieved for various variants of $\hat{P}_l$ (see Supplemental Material, Sec. II [24]). In the following, we use

$\hat{P}_l = \exp[-K/(2r)\hat{m}_l \sum_{|j|=1}^{r} \hat{m}_{l+j}]$. with K denoting the alignment parameter and r defining the interaction radius, which we choose as $r = 4$ in the following. Here, $\hat{m}_l = \hat{n}_{\uparrow l} - \hat{n}_{\downarrow l} = \hat{c}^\dagger_{\uparrow l}\hat{c}_{\uparrow l} - \hat{c}^\dagger_{\downarrow l}\hat{c}_{\downarrow l}$ measures the local magnetization. In analogy to the Vicsek model [16], where each point-agent aligns its velocity direction to the average direction of motion of its neighborhood, our quantum particles align according to their surrounding magnetization.

The Hamiltonian contributes a quantum-coherent real-time evolution through a local spin-flip term $\hat{H} = -g\sum_{l=1}^{L}(\hat{c}^\dagger_{l,\uparrow}\hat{c}_{l,\downarrow} + h.c)$ with g denoting the quantum amplitude. This process provides an inherent (quantum) noise source that counteracts the flock formation. Specifically, the Hamiltonian dynamics randomizes the spin degree of freedom of the particles overcoming at some strength of g the alignment tendency from the dissipative dynamics. Importantly, we will find that this Hamiltonian contribution also qualitatively changes the character of the flock motion inducing a long-distance quantum coherence absent in the classical case.

A key property of the considered model is a $\mathbb{Z}_2$ symmetry by flipping the spins of all particles upon simultaneously reversing the particles' direction of motion, which is the polar symmetry that will be spontaneously broken in the quantum flock. Because of the link between the species type σ and the direction of motion, the collective motion of particles is detectable through the magnetization $\hat{M} = \sum_{l=1}^{L} \hat{m}_l$ as the order parameter.

Long-range order and collective motion—We target the detection of long-range order by means of the Binder cumulant $U(t) = 1 - \langle \hat{M}^4(t)\rangle/(3\langle \hat{M}^2(t)\rangle^2)$ associated to the order parameter $\hat{M}$. Here, $\langle \hat{\mathcal{O}}(t)\rangle = \mathrm{Tr}(\hat{\rho}(t)\hat{\mathcal{O}})$ denotes the time-dependent expectation value of the operator $\hat{\mathcal{O}}$. A more direct measure and visualization of the quantum flock by means of snapshot measurements is introduced below. In the thermodynamic limit, the Binder cumulant is $U = 2/3$ for long-range ordered states whereas $U = 0$ for disordered ones. In Fig. 1(b), we display numerically obtained data for the Binder cumulant $U(t)$ with qualitatively different behavior depending on the strength of the quantum amplitude g. For weak $g/\Gamma = 0.2$, the Binder cumulant rises up to $U(t) \approx 2/3$ for long times with only weak finite-size effects. These results suggest long-range order and the realization of an active quantum flock experiencing collective motion. The behavior is different in the opposite case of large quantum amplitudes $g/\Gamma = 0.8$ where the attained long-time value exhibits a considerable system-size dependence with $U \to 0$ upon increasing L, indicating a disordered phase. We note that all results are obtained at a fixed particle density $\nu = N/L = 1/2$.

In Fig. 1(c), we show the long-time value $\bar{U}$ of the Binder cumulant as a function of g, obtained from a time average in the interval $\Gamma t \in [40, 70]$. We observe compelling evidence for a long-range ordered phase at weak quantum amplitudes $g/\Gamma \ll 1$. For large quantum amplitudes instead, the tendency is clearly toward a disordered state with $\bar{U} \to 0$ upon increasing L. We estimate the phase transition point by identifying the value of g at which $\bar{U}$ crosses a threshold $2/3 - \epsilon$ with $\epsilon = 0.02$, as indicated also in Fig. 1(c). The corresponding estimated phase diagram is shown in Fig. 2. The dashed line in this figure represents the analytical prediction derived from the coarse-grained description of the dynamics in the weak-g limit, presented in the Coarse-Grained Dynamics section. Alternatively, the flocks can also be characterized by the currents generated through the symmetry breaking, as detailed in Sec. II of Supplemental Material [24]. In Sec. III of Supplemental Material [24] we also display further evidence for long-range order in the quantum flocking phase through the real-space magnetization correlation function.

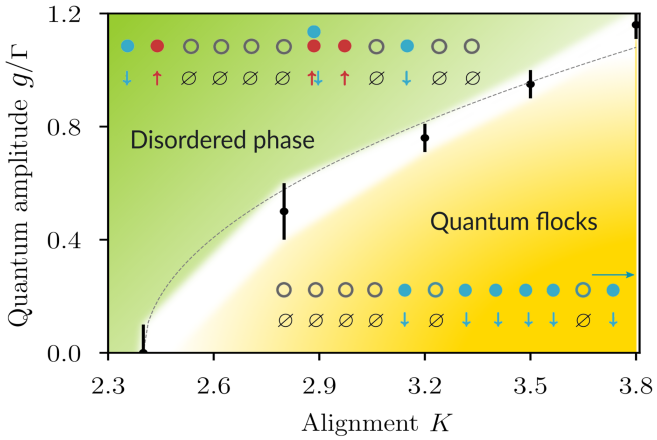

FIG. 2. Phase diagram. Numerically obtained phase diagram with indicated error bars as a function of the alignment parameter K and the quantum amplitude g including representative many-body configurations. The numerical uncertainty for the estimate of the phase transition points is indicated by the white region separating the disordered from the quantum flocking phase. The analytical prediction from the coarse-grained theory at weak quantum amplitudes g is included as a dashed line, which is consistent with the numerical results.

Quantum coherence—A key question remains, namely to what extent quantum flocks differ from those in the classical world. Characterizing such differences is a challenging task, especially in mixed states of quantum matter. While we can identify quantum entanglement in the logarithmic negativity for the quantum flock (see Sec. IV of Supplemental Material [24]) and thereby genuinely quantum behavior, in the following we aim to focus on the quantum coherence [28], which measures the amount of quantum superposition of a general mixed state. We find that the quantum coherence displays the most striking qualitative difference between the quantum flocking and nonflocking phase [see Fig. 3(a)]. Concretely, we consider a total long-distance quantum coherence $C(t) = \sum_{l=1}^{L} C_l(t)$ with $C_l(t) = \sum_{\nu_l \neq \nu_l'} |\langle \nu_l|\hat{\rho}_l^C(t)|\nu_l'\rangle|$, where

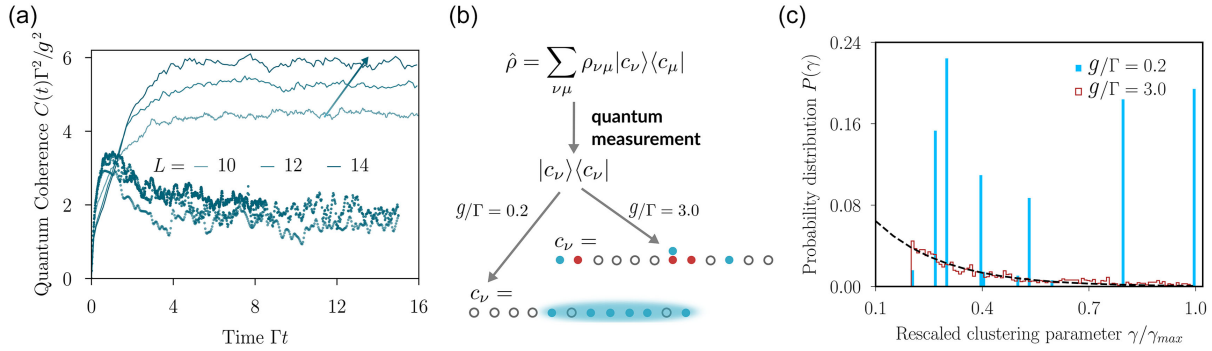

FIG. 3. Quantum coherence and cluster formation. (a) Dynamics of the total long-distance quantum coherence $C(t)$ comparing the flocking phase ($K = 3.8$, solid lines) to the disordered phase ($K = 0.5$, dotted lines) for $g/\Gamma = 0.2$ and different system sizes L calculated for $N_r = 1000$ trajectories. (b) A quantum snapshot measurement on the full density matrix $\hat{\rho}$ yields many-body configurations c_ν with typical outcomes for the quantum flocking ($g/\Gamma = 0.2$) and the disordered phase ($g/\Gamma = 3.0$). (c) Cluster statistics $P(\gamma)$ comparing the quantum flocking ($g/\Gamma = 0.2$) to the disordered phase ($g/\Gamma = 3.0$) at $K = 3.8$ for $N_r = 2000$ trajectories and $L = 12$. Here, $\gamma_{\max} = L^2/4$ denotes the maximally possible γ value.

$\hat{\rho}_l^C(t)$ denotes the reduced density matrix of two lattice sites l and $l + L/2$, i.e., at a maximal distance. The states $|\nu_l\rangle = |\mathbf{n}_l, \mathbf{n}_{l+L/2}\rangle$ represent all the particle configurations with $\mathbf{n}_l = \varnothing, \uparrow, \downarrow, \uparrow\downarrow$. Notice that for a vanishing quantum amplitude $g = 0$ the dynamics reduces to a classical process and to classical flocking without quantum coherence and entanglement. Therefore, we will refer to a quantum flock only for $g > 0$.

In Fig. 3(a), we show our numerical results for $C(t)$ at a fixed quantum amplitude $g/\Gamma = 0.2$. In the disordered phase for weak alignment $K = 0.5$, $C(t)$ settles to a plateau independent of system size L. In the flocking phase instead for large alignment $K = 3.8$, $C(t)$ grows with increasing system size L and time t. Consequently, our numerical simulations suggest that the quantum flock exhibits distinct quantum properties through a long-distance quantum coherence. The obtained results for $C(t)$ also have direct implications for the nature of the collective motion. $C(t)$ is a measure on the strength of the off-diagonal matrix elements in $\rho_l^C(t)$, which involve correlation functions of the form $\langle \hat{c}_{l\uparrow}^\dagger(t)\hat{c}_{l+L/2\uparrow}(t)\rangle$ for instance. This suggests that the quantum flocking state is not only characterized by quantum superposition but also by long-distance quantum-coherent motion.

Alignment and clustering—Having found evidence for intrinsic quantum effects, we aim in a next step to characterize the quantum flock on a microscopic level by means of a clustering analysis [29] extended to snapshot measurements. Such snapshot measurements are obtained by performing a joint projective quantum measurement on each quantum degree of freedom providing as the outcome a single many-body configuration, as accessible on today's quantum simulation or computing platforms [1–4]. Typical snapshots are depicted in Fig. 3(b) pointing toward a fundamental difference between the flocking and disordered phases. Without loss of generality, we focus on the $\sigma = \downarrow$-species with corresponding many-body configurations $\mathbf{n} = (n_{1\downarrow}, n_{2\downarrow}, \ldots, n_{L\downarrow})$ and $n_{l\downarrow} = 0, 1$.

Within the utilized clustering algorithm [29], a clustering parameter $\gamma_l = \varrho_l \delta_l$ is associated to each lattice site l. Here, $\varrho_l = n_{l\sigma} \sum_{|m-l|<d_c} n_{m\sigma}$ denotes a coarse-grained local density, and $\delta_l = \min_{m:\varrho_m > \varrho_l}(|l - m|)$ measures the distance to the next lattice site with higher density. Large clusters can be identified through large values of γ as they exhibit both a high local density ϱ_l and a large distance δ_l [29]. In what follows, we choose $d_c = 4$ for concreteness, and for the site with the highest density we have $\delta_l = L/2$.

In Fig. 3(c), we display the statistics of the clustering parameter γ with $P(\gamma)$ obtained from a histogram. $P(\gamma)$ displays a compelling difference between the two phases. For large quantum amplitudes $g/\Gamma = 3$, we find that $P(\gamma)$ exhibits a monotonically decaying behavior with a strongly suppressed probability for large clusters. In the flocking phase, the picture is qualitatively different. We find a sequence of isolated peaks at large γ values, which represent individual large clusters traveling throughout the system.

Coarse-grained dynamics—Based on the numerical evidence for a quantum flocking phase, it is a key next step to also develop an analytical understanding of our quantum flocking problem. We now present an analysis of a coarse-grained version of the Lindblad master equation, corroborating our numerical findings(see Supplemental Material, Sec. IX for details [24]).

Let us first target a homogeneous solution for the magnetization, $m(t) = \langle \hat{m}_l(t)\rangle$ for all l. We obtain as an exact result $\dot{m}(t) = g\langle \hat{f}\rangle - 2\Gamma_F \langle \hat{P}_l^\dagger \hat{P}_l \hat{m}_l\rangle$ (see End Matter). Here, $\hat{f}(t) = -i[\langle \hat{c}_{l\uparrow}^\dagger(t)\hat{c}_{l\downarrow}(t)\rangle - \langle \hat{c}_{l\uparrow}(t)\hat{c}_{l\downarrow}^\dagger(t)\rangle]$ captures the contribution from the quantum dynamics. In a next step we focus on large times t with $m = \lim_{t\to\infty} m(t)$. Motivated by our numerical simulations suggesting a phase transition, we consider in analogy to a conventional Landau

approach the limit of a small magnetization m, which allows us to perform expansions in powers of m. By means of suitable mean-field factorizations we finally obtain (see End Matter)

$$0 = (K_c - K)m + \frac{4K}{K_c}(Kq - 1)m^3 + \mathcal{O}(m^5). \quad (2)$$

This result is reminiscent of the mean-field solution of the classical Ising model exhibiting a symmetry-broken phase for $K > K_c$ thereby confirming the existence of a quantum flocking phase. Here, $K_c = (1 + \Delta_g/2\sigma_m^2)$, with $\Delta_g = (g^2/2\Gamma^2)$ denoting the shift of the critical point induced by weak quantum amplitudes ($g/\Gamma \ll 1$). This expression is consistent with the numerical results in Fig. 2, where the fitted critical points yield $\sigma_m \approx 0.45$ and confirm the increase of K_c with larger g. In the derivation of Eq. (2) we assume that higher moments of the magnetization can be expanded according to $\langle m^2 \rangle = \langle m \rangle^2 + \sigma_m^2$ and $\langle m^3 \rangle = \langle m \rangle^3 + q\langle m \rangle$. The above effective description is well justified for $r \gg 1$, thereby providing a direct connection to the present coarse-grained theory in a well-controlled limit. Importantly, the quantum flock requires $q > K_c^{-1}$ as the homogeneous solution becomes unstable otherwise (see End Matter). Equation (2) suggests a continuous phase transition for the quantum flocking problem. This aligns with the properties of classical active matter systems in one dimension [30,31].

In view of the Mermin-Wagner-Hohenberg theorem, the finding of long-range order in one dimension might appear remarkable. This, however, can be attributed solely to the active nature of the system and the breaking of local detailed balance. We further corroborate the existence of a long-range ordered state by means of a simulation of a classical analog of the Lindblad master equation, where we also find evidence for a flocking phase for large system sizes. Our coarse-grained theory also supports inhomogeneous solutions for $\Gamma_{\mathcal{A}} > \Gamma_{\mathcal{M}}$, where we observe the formation of traveling wave patterns (see Supplemental Material, Sec. V [24]).

Discussion—In this Letter, we have introduced the concept of active quantum matter. We have formulated a model for active quantum particles giving rise to quantum flocks with distinct quantum features by means of a long-distance quantum coherence.

It is a natural question to which extent the introduced quantum flocks might also be accessible experimentally. In Supplemental Material, Sec. VIII [24], we present experimental schemes to realize in systems of Rydberg atoms the building blocks of the individual processes appearing in the considered Lindblad master equation.

For the future it will be central to further explore the details of the considered model such as to study its density dependence, which is an important control parameter for the classical flocking problem [16,19,20,32–34]. It will be further important to also target more specifically the quantum flocking transition. On the basis of a coarse-grained description we have found evidence for both first-order and continuous transitions depending on the parameter regime. For a numerical approach it would be necessary to explore other advanced numerical methods such as tensor networks [35] or neural quantum states [36,37], as we are operating already at the frontier of what is possible via exact diagonalization. This would also allow us to explore the connection to other long-distance quantum-coherent motion such as in superfluids.

The present Letter paves the way to explore further active quantum matter systems—for instance, by drawing inspiration from the classical side also various other interesting nonequilibrium phases have also been discovered such as motility-induced phase separation [38], active nematics [39], or intermittent collective motion [40–42]. It would also be a natural and promising next step to move toward higher dimensions. Of particular interest would be that higher dimensions might also enable the spontaneous breaking of more complex symmetries than $\mathbb{Z}_2$. Overall, we expect that our Letter will pave the way to yet unexplored nonequilibrium phases of quantum matter with intriguing properties.

Acknowledgments—We acknowledge valuable discussions with Ricard Alert, Rainer Blatt, Alexander Eisfeld, Juan Garrahan, Michael Knap, Igor Lesanovsky, Frank Pollmann, Achim Rosch, and Johannes Zeiher. This project has received funding from the European Research Council (ERC) under the European Union's Horizon 2020 research and innovation programme (Grant Agreement No. 853443), and M. H. further acknowledges support by the Deutsche Forschungsgemeinschaft via the Gottfried Wilhelm Leibniz Prize program. Parts of the numerical simulations were performed at the Max Planck Computing and Data Facility in Garching.

Data availability—The data displayed in the figures is available on [43].

[1] C. Gross and I. Bloch, Science **357**, 995 (2017).
[2] C. Monroe, W. C. Campbell, L. M. Duan, Z. X. Gong, A. V. Gorshkov, P. W. Hess, R. Islam, K. Kim, N. M. Linke, G. Pagano, P. Richerme, C. Senko, and N. Y. Yao, Rev. Mod. Phys. **93**, 025001 (2021).
[3] A. Browaeys and T. Lahaye, Nat. Phys. **16**, 132 (2020).
[4] A. Blais, A. L. Grimsmo, S. M. Girvin, and A. Wallraff, Rev. Mod. Phys. **93**, 025005 (2021).
[5] M. Schreiber, S. S. Hodgman, P. Bordia, H. P. Lüschen, M. H. Fischer, R. Vosk, E. Altman, U. Schneider, and I. Bloch, Science **349**, 842 (2015).
[6] J. Smith, A. Lee, P. Richerme, B. Neyenhuis, P. W. Hess, P. Hauke, M. Heyl, D. A. Huse, and C. Monroe, Nat. Phys. **12**, 907 (2016).

[7] S. Choi, J. Choi, R. Landig, G. Kucsko, H. Zhou, J. Isoya, F. Jelezko, S. Onoda, H. Sumiya, V. Khemani, C. von Keyserlingk, N. Y. Yao, E. Demler, and M. D. Lukin, Nature (London) **543**, 221 (2017).
[8] J. Zhang, P. W. Hess, A. Kyprianidis, P. Becker, A. Lee, J. Smith, G. Pagano, I. D. Potirniche, A. C. Potter, A. Vishwanath, N. Y. Yao, and C. Monroe, Nature (London) **543**, 217 (2017).
[9] H. Bernien, S. Schwartz, A. Keesling, H. Levine, A. Omran, H. Pichler, S. Choi, A. S. Zibrov, M. Endres, M. Greiner, V. Vuletić, and M. D. Lukin, Nature (London) **551**, 579 (2017).
[10] F. Jülicher, A. Ajdari, and J. Prost, Rev. Mod. Phys. **69**, 1269 (1997).
[11] S. Ramaswamy, Annu. Rev. Condens. Matter Phys. **1**, 323 (2010).
[12] M. C. Marchetti, J.-F. Joanny, S. Ramaswamy, T. B. Liverpool, J. Prost, M. Rao, and R. A. Simha, Rev. Mod. Phys. **85**, 1143 (2013).
[13] J. Prost, F. Jülicher, and J.-F. Joanny, Nat. Phys. **11**, 111 (2015).
[14] M. E. Cates and E. Tjhung, J. Fluid Mech. **836**, P1 (2018).
[15] C. A. Weber, D. Zwicker, F. Jülicher, and C. F. Lee, Rep. Prog. Phys. **82**, 064601 (2019).
[16] T. Vicsek, A. Czirók, E. Ben-Jacob, I. Cohen, and O. Shochet, Phys. Rev. Lett. **75**, 1226 (1995).
[17] J. Toner, Y. Tu, and S. Ramaswamy, Ann. Phys. (Amsterdam) **318**, 170 (2005).
[18] H. Chaté, Annu. Rev. Condens. Matter Phys. **11**, 189 (2020).
[19] A. P. Solon and J. Tailleur, Phys. Rev. Lett. **111**, 078101 (2013).
[20] A. P. Solon and J. Tailleur, Phys. Rev. E **92**, 042119 (2015).
[21] C. A. Weber, C. Bock, and E. Frey, Phys. Rev. Lett. **112**, 168301 (2014).
[22] É. Fodor, R. L. Jack, and M. E. Cates, Annu. Rev. Condens. Matter Phys. **13**, 215 (2022).
[23] M. Bär, R. Großmann, S. Heidenreich, and F. Peruani, Annu. Rev. Condens. Matter Phys. **11**, 441 (2020).
[24] See Supplemental Material at http://link.aps.org/supplemental/10.1103/rd46-hr3q for additional derivations, current fluctuations, correlation functions, entanglement analysis, a classical analogue of the model, coarse-grained hydrodynamics, and experimental implementation details.
[25] C. Gardiner and P. Zoller, *Quantum Noise: A Handbook of Markovian and Non-Markovian Quantum Stochastic Methods with Applications to Quantum Optics* (Springer Science & Business Media, New York, 2004).
[26] A. P. Antonov, Y. Zheng, B. Liebchen, and H. Löwen, Phys. Rev. Res. **7**, 033008 (2025).
[27] M. Yamagishi, N. Hatano, and H. Obuse, Sci. Rep. **14**, 28648 (2024).
[28] A. Streltsov, G. Adesso, and M. B. Plenio, Rev. Mod. Phys. **89**, 041003 (2017).
[29] A. Rodriguez and A. Laio, Science **344**, 1492 (2014).
[30] A. Czirók, A.-L. Barabási, and T. Vicsek, Phys. Rev. Lett. **82**, 209 (1999).
[31] O. O'Loan and M. Evans, J. Phys. A **32**, L99 (1999).
[32] E. Bertin, M. Droz, and G. Grégoire, J. Phys. A **42**, 445001 (2009).
[33] C. A. Weber, V. Schaller, A. R. Bausch, and E. Frey, Phys. Rev. E **86**, 030901 (2012).
[34] C. A. Weber, F. Thüroff, and E. Frey, New J. Phys. **15**, 045014 (2013).
[35] R. Orús, Nat. Rev. Phys. **1**, 538 (2019).
[36] G. Carleo and M. Troyer, Science **355**, 602 (2017).
[37] M. Schmitt and M. Heyl, Phys. Rev. Lett. **125**, 100503 (2020).
[38] M. E. Cates and J. Tailleur, Annu. Rev. Condens. Matter Phys. **6**, 219 (2015).
[39] L. Giomi, Phys. Rev. X **5**, 031003 (2015).
[40] C. Huepe and M. Aldana, Phys. Rev. Lett. **92**, 168701 (2004).
[41] A. Cavagna, I. Giardina, and F. Ginelli, Phys. Rev. Lett. **110**, 168107 (2013).
[42] L. Gómez-Nava, R. Bon, and F. Peruani, Nat. Phys. **18**, 1494 (2022).
[43] R. Khasseh, Active quantum flocks (data set), Zenodo, Version v110.5281/zenodo.8208685 (2023).
[44] G. Schaller, *Open Quantum Systems Far from Equilibrium* (Springer, New York, 2014), Vol. 881.
[45] G. M. Schütz, J. Phys. A **36**, R339 (2003).

End Matter

Numerical solution of the Lindblad master equation—We solve the Lindblad master equation via exact diagonalization through a mapping to a stochastic Schrödinger equation. We achieve up to $L = 14$ lattice sites, which on the level of the Lindblad equation corresponds to solve 10^{12} coupled first-order differential equations. In our simulations, we choose for convenience $\Gamma_{\mathcal{M}} = \Gamma_{\mathcal{A}} = \Gamma$, and we consider initial conditions $|\psi_0\rangle$ with a vanishing magnetization and short-range correlations, $|\psi_0\rangle = \otimes_{l=1}^{N} |\psi_0\rangle_l \otimes_{l=N+1}^{L} |0\rangle_l$, where $|\psi_0\rangle_l = 2^{-1/2}(|\uparrow\rangle_l + |\downarrow\rangle_l)$ and $|0\rangle_l$ denotes an empty lattice site. We verified that the properties of the steady state do not depend on the choice of the initial condition (see Supplemental Material, Sec. VII [24]). The initial condition sets the density $\nu = N/L = 1/2$ of particles in the system.

We solve numerically the Lindblad master equation in Eq. (1) as a piecewise deterministic process. Instead of calculating the full dynamics of the density matrix $\hat{\rho}(t)$, we sample pure-state trajectories $|\psi_t(z)\rangle$ in Hilbert space according to a probability distribution such that we recover $\hat{\rho}_t$ as an average over the individual trajectories [44], i.e.,

$$\rho_t = \mathcal{M}\{|\psi_t(z)\rangle\langle\psi_t(z)|\}, \tag{A1}$$

where z refers to a suitably chosen stochastic process. The evolution of the system can then be effectively

modeled by [44]

$$|d\psi\rangle = \hat{H}_{\text{eff}}|\psi\rangle dt + \sum_{l,\sigma}\left(\frac{\hat{\mathcal{M}}_{l,\sigma}|\psi\rangle}{\sqrt{\langle\psi|\hat{\mathcal{M}}^\dagger_{l,\sigma}\hat{\mathcal{M}}_{l,\sigma}|\psi\rangle}} - |\psi\rangle\right) dN^{\mathcal{M}}_{l,\sigma} + \sum_{l,\sigma}\left(\frac{\hat{\mathcal{A}}_{l,\sigma}|\psi\rangle}{\sqrt{\langle\psi|\hat{\mathcal{A}}^\dagger_{l,\sigma}\hat{\mathcal{A}}_{l,\sigma}|\psi\rangle}} - |\psi\rangle\right) dN^{\mathcal{A}}_{l,\sigma}, \tag{A2}$$

and therefore by a nonlinear stochastic Schrödinger equation. The effective non-Hermitian Hamiltonian reads as [44]

$$\hat{H}_{\text{eff}} = -iH - \frac{\Gamma_{\mathcal{M}}}{2}\sum_{l,\sigma}\hat{\mathcal{M}}^\dagger_{l,\sigma}\hat{\mathcal{M}}_{l,\sigma} - \frac{\Gamma_{\mathcal{A}}}{2}\sum_{l,\sigma}\hat{\mathcal{A}}^\dagger_{l,\sigma}\hat{\mathcal{A}}_{l,\sigma} + \frac{\Gamma_L}{2}\sum_{l,\sigma}\langle\psi|\hat{\mathcal{M}}^\dagger_{l,\sigma}\hat{\mathcal{M}}_{l,\sigma}|\psi\rangle + \frac{\Gamma_{\mathcal{A}}}{2}\sum_{l,\sigma}\langle\psi|\hat{\mathcal{A}}^\dagger_{l,\sigma}\hat{\mathcal{A}}_{l,\sigma}|\psi\rangle. \tag{A3}$$

The Poisson increments $dN^X_{l,\sigma}$ satisfy

$$dN^X_\alpha dN^X_\beta = \delta_{\alpha\beta}dN^X_\alpha, \quad M(dN^X_\alpha) = \Gamma_X\langle\psi|\hat{X}^\dagger_\alpha\hat{X}_\alpha|\psi\rangle, \tag{A4}$$

where $M(X)$ indicates the classical average over the trajectory ensemble, and dN^X_α can be $\{0,1\}$. Equation (A4) implies that we have at most one single jump at each time step t occurring with probability $P_\alpha = \sum_x \Gamma_X\langle\psi|\hat{X}^\dagger_\alpha\hat{X}_\alpha|\psi\rangle dt$. On a general level, the stochastic differential equation in Eq. (A2) represents a combination of a deterministic evolution and stochastic quantum jumps. The stochastic part we solve as follows. First, at a given time t, we evaluate for the next time step the total jump probability during the interval $[t, t+\Delta t]$ with Δt a small time interval. Based on that probability we randomly decide for the occurrence of a jump. In case a jump is supposed to take place, we further randomly select the type of the jump, which is then finally executed. In the opposite case of no jump, we replace $dN_\alpha = 0$ for all α in Eq. (A2) and solve the resulting deterministic nonlinear differential equation to determine $|\psi(t+\Delta t)\rangle$ at the next step. This procedure is then iterated over time in order to obtain a full trajectory of the quantum many-body state $|\psi_t(z)\rangle$. In the end we average over N_r such trajectories to calculate expectation values of observables.

Coarse-grained dynamics—Here, we provide details on the derivation of the coarse-grained equations of motion obtained from the Lindblad master equation. The local occupation numbers $\hat{n}_{l,\sigma} = \hat{c}^\dagger_{l\sigma}\hat{c}_{l\sigma}$ obey the following general expression:

$$\frac{d}{dt}\langle\hat{n}_{l,\sigma}\rangle = \sigma g\langle\hat{f}_l\rangle + \Gamma_{\mathcal{A}}\langle\hat{P}^\dagger_l\hat{P}_l(\hat{n}_{l\bar{\sigma}} - \hat{n}_{l\sigma})\rangle + \Gamma_{\mathcal{M}}\left[\langle\hat{n}_{l+\sigma,\sigma}(1-\hat{n}_{l,\sigma})\rangle - \langle(1-\hat{n}_{l-\sigma,\sigma})\hat{n}_{l,\sigma}\rangle\right] \tag{B1}$$

with $\sigma = \uparrow, \downarrow$ and $\bar{\sigma}$ being the complement of σ. In the spatial index we also use $\uparrow/\downarrow = \pm 1$, and $\hat{f}_l = i(\hat{c}^\dagger_{l\uparrow}\hat{c}_{l\downarrow} - \hat{c}_{l\uparrow}\hat{c}^\dagger_{l\downarrow})$ is the local spin-flip current operator.

Interestingly, Eq. (7) reproduces the classical TASEP dynamics in the limit $g, \Gamma_F \to 0$ [45]. From Eq. (7) we derive the equations of motion for the local densities $\hat{\rho}_l = (\hat{n}_{l\uparrow} + \hat{n}_{l\downarrow})/2$ and magnetizations $\hat{m}_l = (\hat{n}_{l\uparrow} - \hat{n}_{l\downarrow})/2$, viz.,

$$\frac{d}{dt}\langle\hat{\rho}_l\rangle = \Gamma_{\mathcal{M}}\left[\left\langle\left(\frac{1}{2} - \hat{\rho}_l\right)\delta\hat{m}_l\right\rangle - \langle\hat{m}_l\delta\hat{\rho}_l\rangle + \frac{\langle\delta^2\hat{\rho}_l\rangle}{2}\right] \tag{B2}$$

$$\frac{d}{dt}\langle\hat{m}_l\rangle = g\langle\hat{f}_l\rangle - 2\Gamma_{\mathcal{A}}\langle\hat{P}^\dagger_l\hat{P}_l\hat{m}_l\rangle - \Gamma_{\mathcal{M}}\left[\left\langle\left(\hat{\rho}_l - \frac{1}{2}\right)\delta\hat{\rho}_l\right\rangle + \langle\hat{m}_l\delta\hat{m}_l\rangle - \frac{\langle\delta^2\hat{m}_l\rangle}{2}\right] \tag{B3}$$

$$\frac{d}{dt}\langle\hat{f}_l\rangle = -4g\langle\hat{m}_l\rangle - \frac{\Gamma_{\mathcal{A}}}{2}\langle\{\hat{P}^\dagger_l\hat{P}_l, \hat{f}_l\}\rangle - \Gamma_{\mathcal{M}}\langle(1+\delta\hat{m}_l)\hat{f}_l\rangle \tag{B4}$$

with the finite differences $\delta\mathcal{O}_l = \mathcal{O}_{l+1} - \mathcal{O}_{l-1}$ and $\delta^2\mathcal{O}_l = \mathcal{O}_{l+1} + \mathcal{O}_{l-1} - 2\mathcal{O}_l$. In the remainder, we assume $[\hat{P}^\dagger_l\hat{P}, \hat{f}_l] = 0$, which is true, e.g., when $\hat{P}^\dagger_l\hat{P}_l$ is a function of the local magnetizations.

Homogeneous mean-field solution—First, we study homogeneous solutions of Eqs. (B2)–(B4) where $m(t) = \langle\hat{m}_l(t)\rangle$ and $\rho(t) = \langle\hat{\rho}_l(t)\rangle$ for all l. Upon factorizing the term proportional to $\Gamma_{\mathcal{M}}$ in a mean-field way for all correlations, Eq. (B3) reads:

$$\frac{d}{dt}m(t) = gf(t) - 2\Gamma_{\mathcal{A}}\langle\hat{P}^\dagger_l(t)\hat{P}_l(t)\hat{m}_l(t)\rangle. \tag{C1}$$

Here, we address the nonlinearity $\langle\hat{P}^\dagger_l(t)\hat{P}_l(t)\hat{m}_l(t)\rangle$ by using the explicit form of the alignment operator $\hat{P}^\dagger_l\hat{P}_l = \exp(-2K\hat{m}_l\hat{M}^l)$, with $\hat{M}^l = L^{-1}\sum_{j\neq l}\hat{m}_j$. This corresponds to the alignment operator in the main text for $r = L/2$. In analogy to a conventional Landau description of the phase transition, we capture the onset of order using a Taylor-expansion in powers of the magnetization:,

$$\langle\hat{m}_l\hat{P}^\dagger_l\hat{P}_l\rangle \simeq m - 2K\langle\hat{m}^2_l\hat{M}^l\rangle + 2K^2\langle\hat{m}^3_l\hat{M}^l\hat{M}^l\rangle. \tag{C2}$$

Next, we address the factorization of the remaining higher-order correlations. To this end, we consider

all local magnetizations as independently fluctuating, uncorrelated quantities. As $\hat{M}^l$ is a mean magnetization, we expect its fluctuations to be subleading for large system sizes and thus neglect them. We then find

$$\langle \hat{m}_l P_l^\dagger P_l \rangle \simeq m - 2K\langle \hat{m}_l^2 \rangle m + 2K^2 \langle \hat{m}_l^3 \rangle m^2, \quad \text{(C3)}$$

where we have used $\langle \hat{M}^l \rangle = m$ for the targeted homogeneous solution. Thus, the higher moments of the local magnetization remain to be considered. We expand these in terms of lower-order moments according to.

$\langle \hat{m}_l^2 \rangle = m^2 + \sigma^2$ and $\langle \hat{m}_l^3 \rangle = m^3 + qm$, with σ^2 and q some constants, whose exact values would have to be derived from microscopic considerations. Consequently, for $g = 0$, we obtain for the stationary steady state solution

$$\frac{dm}{dt} = 0 = m^4 + \left[q - \frac{1}{K}\right] m^2 + \frac{1}{2K^2} - \frac{\sigma^2}{K}. \quad \text{(C4)}$$

For the onset of the flocking phase with $|m| \ll 1$, we can neglect the contributions of the order m^4 yielding

$$m^2 \simeq \frac{1}{2K_c^2} \frac{K/K_c - 1}{q - 1/K_c} \quad \text{(C5)}$$

with the critical value $K_c = 1/(2\sigma^2)$. This equation exhibits its solutions along two distinct branches—one for $K > K_c$ with $q > 1/K_c$ and the other for $K < K_c$ with $q < 1/K_c$. As we show now, only one of these is stable. We consider a weak, and still homogeneous, time-dependent deviation $u(t)$ on top of the homogeneous solution, i.e., $m = m_0 + u(t)$. We find for the dynamics of the deviation to leading order

$$\frac{du}{dt} = -4\Gamma_{\mathcal{A}} \left(\frac{K}{K_c} - 1 \right) u, \quad \text{(C6)}$$

which clearly indicates that only the solution with $K > K_c$ and $q > 1/K_c$ is stable.

Lastly, we consider the influence of the quantum dynamics of amplitude g on the homogeneous solution (C5). The quantum dynamics couples Eqs. (B3) and (B4). In the stationary state we find the homogeneous transverse current $f \simeq -4gm/(\Gamma_{\mathcal{M}} + \Gamma_{\mathcal{A}})$. Hence, the homogeneous solution is altered as follows:

$$m^2 \simeq \frac{1}{2K_c^2} \frac{K/K_c - 1 - \Delta_g}{q - 1/K_c} \quad \text{(C7)}$$

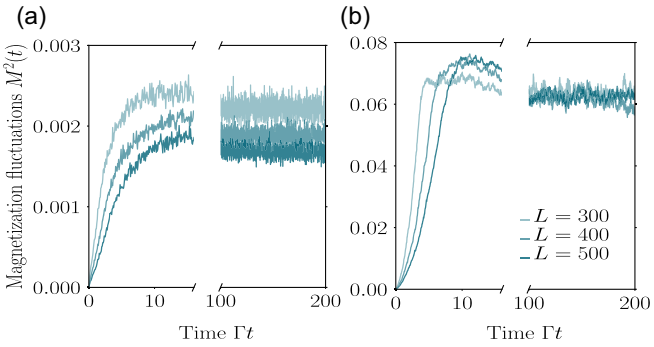

FIG. 4. Classical analog of the quantum flocking problem. Dynamics of magnetization fluctuations $M^2(t)$ for the alignment parameter $K = 0.5$ in (a) and $K = 3.5$ in (b).

with $\Delta_g = 4g^2/[\Gamma_{\mathcal{A}}(\Gamma_{\mathcal{M}} + \Gamma_{\mathcal{A}})]$. In particular we find that the quantum dynamics shifts the critical point as $K_c(g) \simeq (1 + \Delta_g) K_c(g = 0)$. Since $\Delta_g > 0$, larger coupling strengths are required to induce order, which is consistent with the exact numerical data for the phase diagram. In Supplemental Material [24] we further discuss the inhomogeneous solutions provided by the coarse-grained description yielding also traveling wave patterns.

Classical limit—Our flocking model discussed in the main text exhibits a classical limit for $g \to 0$. In this limit, the coherent spin-flip dynamics generated by the Hamiltonian is absent, leaving behind purely stochastic processes: biased hopping, alignment interactions, and effective noise. While the quantum model features coherent and dissipative competition, the classical counterpart consists solely of probabilistic jump processes, making it also computationally simple.

The behavior of the classical model concerning flocking is similar to the quantum case. In Fig. 4, we simulate the evolution of the order parameter fluctuations M^2 for two values of the alignment strength, $K = 0.5$ and $K = 3.5$, and various system sizes L. For weak alignment ($K = 0.5$), the long-time value of M^2 decreases with increasing L, indicating the absence of long-range order. In contrast, for strong alignment ($K = 3.5$), M^2 remains finite as L increases, signaling the emergence of a stable, symmetry-broken phase with global magnetization—the classical case of flocking. These results demonstrate that also in the absence of coherent dynamics, the essential ingredients of flocking—directional motion and alignment—are sufficient to induce collective behavior. Additional numerical data are provided in Supplemental Material [24].